Comparisons between Thermal Modeling and Experiments in Laser-Densified Dental Powder Bodies

Kun Dai, Xiaoxuan Li, Leon L. Shaw
Department of Metallurgy and Materials Engineering
Institute of Materials Science
University of Connecticut
Storrs, CT 06269, USA

Abstract

A three-dimensional thermal finite element model including the effect of the powder-to-solid transition has been developed to investigate the transient temperature distribution during laser densification of dental powder bed for the layer-by-layer fabrication. The model encompasses the effects of the temperature- and porosity-dependent thermal conduction and radiation as well as the temperature-dependent natural convection. The simulation result is compared with the experiments which establish the temperature dependence of the dental porcelain microstructure and utilize this dependence to construct the temperature distribution profile. It is found that the trend of the simulation result matches the experiments very well.

Keywords: Dental restoration, Laser processing, Finite element modeling, Thermal analyses, Powder melting and solidification.

I. Introduction

Solid freeform fabrication (SFF) is an automated manufacturing process that builds three-dimensional complex-shaped structures layer-by-layer directly from CAD data [1]. The recent advancement of SFF has led to a multi-material laser densification (MMLD) process for dental restoration [2-4]. Through this approach artificial teeth are expected to be fabricated from a computer model without part-specific tooling and human intervention, thereby offering the potential to reduce the labor cost and increase the restoration rate. However, as the densification of the dental porcelain powder is accomplished via a laser beam, an understanding of the temperature distribution in the laser-assisted densification process is necessary in order to understand the phase transformation and microstructural evolution of the dental porcelain powder during laser densification. The understanding developed will provide the guideline to optimize the laser processing condition so that the microstructure and thus the mechanical properties of the laser-densified bodies are similar to those obtained via traditional furnace annealing process. The approach of finite element modeling (FEM) has been taken in this study to investigate the temperature distribution during laser densification. The FEM approach is necessary because the relative density of the workpiece changes continuously with time during

laser densification until it reaches near full density. As a result, the thermal conductivity of the workpiece also changes continuously. Thus, the transient temperature field of the workpiece is too complex to calculate using analytical methods, and numerical simulation becomes necessary.

Many numerical modeling efforts have been carried out to investigate the temperature field in various SFF processes [5-22]. However, they are not suitable for the laser-assisted dental restoration process which requires the numerical models to encompass at least the effects of the powder-to-solid transition, laser power density, closed-loop temperature control, temperature-dependent thermal convection, and temperature- and porosity-dependent thermal conduction and radiation. Most of the existing SFF models (e.g., Refs. 5 – 22) are not so sophisticated. Therefore, in this study we have developed a model that includes (i) a coupled-filed analysis between temperature and porosity fields, (ii) the incoming laser beam power with Gaussian distribution, (iii) the optical pyrometer simulation in addition to the closed-loop temperature control, (iv) powder-to-solid transition, (v) temperature-dependent thermal convection, and (vi) temperature- and porosity-dependent thermal conduction and radiation. The results from the numerical simulation have been compared with experiments and found to match the experimental measurements quite well.

II. Model Description

The model developed is shown in Figure 1 and consists of a dental porcelain powder compact with a dimension of 10mm length, 6mm width and 2mm height before laser densification. In simulation the laser beam is modeled as a heat flux, Q, with a Gaussian power distribution as an incoming heat source, which moves at a constant rate (240 μm/s) along the X-axis as shown in Figure 1. The heat losses from the six surfaces of the model are assumed to result from thermal natural convection and the radiation. The dental porcelain powder is composed of 63.40% SiO_2, 16.70% Al_2O_3, 1.50% CaO, 0.80% MgO, 3.41% Na_2O, and 14.19% K_2O (wt%). The material thermal properties for the dense solid porcelain used in the model are summarized in Table 1. The dental porcelain is assumed to be at a molten state above 1073K (100K higher than the lower temperature of the forming temperature range of the porcelain) and no volume shrinkage is considered when powder porcelain converts to dense porcelain.

The modeling is carried out using the ANSYS commercial finite element package. The thermal element (Solid70), which has eight nodes with a single degree of freedom (*i.e.*, temperature) at each node and has a 3D thermal-conduction capability, is used to simulate the temperature field [23]. Each element near the surface has a size of 0.25 mm length, 0.25 mm width and 0.2 mm height. The model is first used to calculate the temperature distribution in the powder bed within a small time step resulting from the heating of a laser beam moving at a constant rate along the X-axis. The powder elements convert to dense molten elements if their temperatures are higher than 1073K according to the calculated temperature field, and the temperature distribution in the powder bed within the next small time step is calculated using the updated material properties. This simulation loop continues until the total amount of the small time steps, which is decided by the laser scanning rate, is reached, and then the laser beam moves stepwise by one element to carry out the next simulation loop. The substrate preheating is

achieved in the simulation by assigning an elevated temperature (460^0C) as the nodal temperature of the bottom surface.
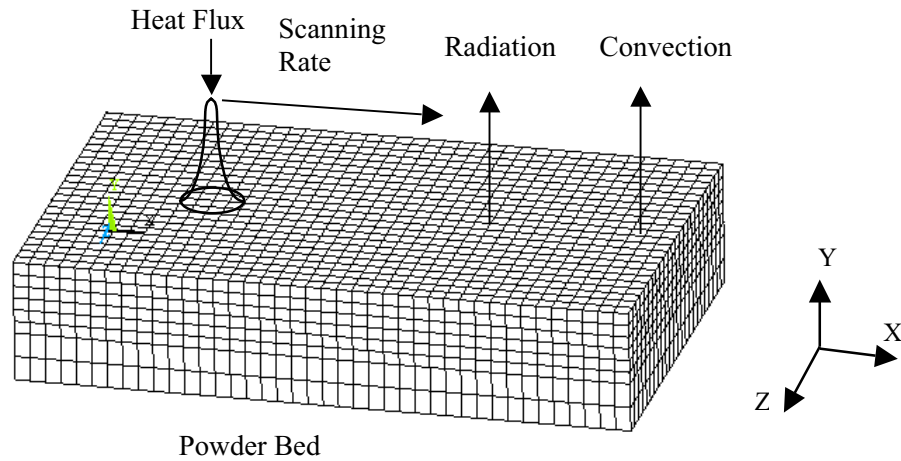

Figure 1. Finite element model developed to simulate the temperature field during laser densification of the dental porcelain body.

Table 1. Summary of Thermal Properties of Dental Porcelain [24 – 28]

T (K)	300	520	631	700	830	960	1173	1373	1540	1726	1730	1800
k (W/m-K)	1.11	1.37	1.55	1.67	1.93	2.23	2.82	2.82	2.82	2.82	2.82	2.82
C_p (J/kg-K)	742	1025	1125	1178	1266	1341	1444	1474	1474	1474	1474	1474
α (10^{-6}/K)	2.80	3.36	3.87	4.27	5.25	6.54	9.43	9.43	9.43	9.43	9.43	9.43
E (GPa)	70	55.6	48.4	43.9	35.4	26.9	—	—	—	—	—	—
ε						0.7						
ρ (kg/m^3)						2520						
T_m (K)						1573						
T_f (K)						973 to1273						
ν						0.2						

*T–Temperature, k–Thermal Conductivity, C_p–Specific Heat, α–Thermal Expansion Coefficient, E – Elastic Modulus, ε –Emissivity, ρ –Density, T_m – Melting Temperature, T_f – Forming temperature, ν –Poisson's Ratio.

The thermal properties of the powder bed are a strong function of the porosity of the powder bed. It is assumed that the porosity of the powder bed is temperature independent before the powder becomes liquid. This is a reasonable assumption because the reduction in porosity due to solid-state sintering is minimal under the present laser densification condition which brings the local temperature of the area irradiated by the laser beam to above the forming temperature of the porcelain in less than 6 seconds. For the region outside the irradiated area, the time for the region to expose to high temperatures is also relatively short (less than 100 seconds) because of the scanning rate used. Furthermore, the temperature at the region outside the irradiated area is also relatively low because of the low thermal conductivity of the powder compact. As such, the porosity of material has been simplified in two levels, that is, the initial porosity φ_0 before the powder converts to liquid, and zero porosity (fully dense) after the powder

has converted to liquid. The thermal properties of the powder bed, therefore, are treated as a function of temperature and the initial porosity φ_0. The details of these functions and thermal boundary conditions can be found in a recent paper [21] and described briefly as follows.

A. Thermal Conductivity of the Powder Bed

Effective thermal conductivity of the powder bed, k, is estimated by Equation (1) with the assumption that the particles are spheres and there is no flattening of contact surfaces [29].

$$\frac{k}{k_f} = (1 - \sqrt{1-\varphi_0})(1 + \frac{\varphi_0 k_r}{k_f}) + \sqrt{1-\varphi_0}\left(\frac{2}{1 - \frac{k_f}{k_s}}\left(\frac{1}{1 - \frac{k_f}{k_s}}\ln\left(\frac{k_s}{k_f}\right) - 1 \right) + \frac{k_r}{k_f} \right) \quad (1)$$

Where, k_f and k_s are the thermal conductivities of the ambient air and solid particle, respectively; k_r is the thermal conductivity portion of the powder bed due to radiation among particles and equals to [29,30]

$$k_r = 4F\sigma T^3 x_r \quad (2)$$

where σ is the Stefan-Boltzmann constant, x_r is the average diameter of the powder particles, T is the temperature of powder particles, and F is a view factor which is approximately taken as 1/3 [30].

B. Thermal Radiation of the Powder Bed

The emissivity of the powder bed, ε, is obtained by

$$\varepsilon = A_H \varepsilon_H + (1 - A_H)\varepsilon_S \quad (3)$$

where, A_H is the area fraction of the surface that is occupied by the radiation-emitting holes, ε_S and ε_H are the emissivities of solid particle and hole, respectively. For a powder bed composed of randomly packed, single-sized spheres, A_H and ε_H are given by [31]

$$A_H = \frac{0.908\varphi_0^2}{1.908\varphi_0^2 - 2\varphi_0 + 1} \quad (4)$$

and

$$\varepsilon_H = \frac{\varepsilon_S \left[2 + 3.082(\frac{1-\varphi_0}{\varphi_0})^2 \right]}{\varepsilon_S \left[1 + 3.082(\frac{1-\varphi_0}{\varphi_0})^2 \right] + 1} \quad (5)$$

C. Thermal Convection around the Powder Bed

The heat transfer coefficient, h_c, is temperature and size dependent [32]

$$h_c = \frac{N_u k_f}{L} \tag{6}$$

where L is the characteristic length of the specimen, N_u is the Nusselt number, and k_f is the thermal conductivity of the fluid as defined before. N_u is given by [33]

$$\sqrt{N_u} = \sqrt{N_{u0}} + \left[\frac{G_r P_r / 300}{(1 + (0.5/P_r)^{9/16})^{16/9}} \right]^{1/6} \tag{7}$$

when $10^{-4} \leq G_r P_r \leq 4 \times 10^{14}$, $0.022 \leq P_r \leq 7640$, and $N_{u0} = 0.67$ for a plate [33]. G_r and P_r in Equation (7) are Grashof and Prandtl numbers, respectively [32].

$$G_r = g \frac{L^3 \rho_f^2 \beta_f (T - T_{amb})}{\eta_f^2} \tag{8}$$

and

$$P_r = \frac{C_p \eta_f}{k_f} \tag{9}$$

where g is the gravitational acceleration, ρ_f is the density of the ambient air, β_f is the thermal volumetric expansivity and $\beta_f = 1/T_f$ for idea gases, η_f is the viscosity of the air, C_p is the specific heat of the air. The effect of the variation of air properties with temperature is evaluated at $T_f = 0.5(T + T_{amb})$, where T is the surface temperature of the powder bed, T_{amb} is the ambient temperature [32].

D. Thermal Boundary Conditions for Powder, Liquid and Solid

The part being built is assumed to be in contact with air and the heat loss through air is approximated through the natural thermal convection and thermal radiation between the part and the ambient air. Since the model includes three kinds of material status (i.e., powder, liquid and solid), the thermal boundary conditions are very complicated and vary with porosity, phase status and surface temperature which is the function of incident laser power and laser scanning rate. Under the assumption of little convection of liquid within the molten pool due to its small size (~ 2 mm), liquid and solid have been assumed to have the same thermal convection boundary as the powder bed, i.e., thermal convection around the surface of liquid pool and solid is determined by the temperatures of the ambient air and the liquid and solid under consideration [see eqs. (6-9)]. Heat loss q_r due to radiation of solid and liquid is described by [32]

$$q_r = \sigma \varepsilon_s \left(T^4 - T_{amb}^4 \right) \tag{10}$$

where T is the surface temperature of solid and liquid, and ε_s is the emissivity of the dense porcelain, T_{amb} is the ambient temperature, and σ is the Stefan-Boltzmann constant.

The model of a moving Gaussian distribution laser beam, pyrometer temperature simulation, closed-loop temperature control of the laser power are described in detail in the paper [20] and is described as follows.

E. Heat Input

The heat flux of the laser beam, Q, is related to the power of the laser beam, *P*, through the following relation [34]:

$$Q = \frac{2P\alpha_a}{\pi r_0^2} e^{-\frac{2r^2}{r_0^2}} \tag{11}$$

where α_a is the absorptivity of the workpiece, r_0 is the radius of the laser beam at which the heat flux value is e^{-2} times of that of the laser beam center, and r is the distance of a point on the surface of the powder bed measured from the laser beam center. When the center of the laser beam scans the surface of the powder bed from the starting point (X_0, Y_0, Z_0) to (X, Y_0, Z_0) point along the positive X-direction with a constant velocity *V* for a period time *t*, *r* is given by

$$r^2 = (X - X_0 - Vt)^2 + (Z - Z_0)^2 \tag{12}$$

In the present study, the radius of the incident laser beam, r_0, is 0.5 mm, the laser scanning velocity, V, is 0.24 mm/s. The absorptivity of the dental porcelain workpiece, α_a, was varied in the simulation, and a value of 0.41 was needed for the simulated laser input power to match the experimental values. This absorptivity value is comparable with experimental scatter for measured values of α_a for sintered SiC near the processing temperatures used here [35].

F. Pyrometer Simulation

In laser-densification experiments, an optical pyrometer continually monitors the temperature distribution at the surface of the powder bed during laser densification. This pyrometer temperature is used as the feedback signal in a closed-loop control program to adjust the incident laser power as needed to achieve a desired constant laser spot temperature. In the simulation, the pyrometer temperature measurement and the closed-loop control process are modeled as follows.

The power, E, of the thermal radiation emitted by the laser-heated workpiece that reaches the pyrometer can be expressed by [35]

$$E = \int I(\lambda, T) \Delta \lambda dA \tag{13}$$

where λ is the wavelength of the emitted radiation , $\Delta \lambda$ is the wavelength band of the emitted radiation that is sampled by the pyrometer, *T* is the temperature at a very small area *dA* through which the radiation passes to reach the pyrometer, termed the pyrometer sampling area hereafter, $I(\lambda, T)$ is the spectral distribution of blackbody emissive power and given by Planck's radiation law [36]:

$$I(\lambda, T) = \frac{2\pi hc^2}{\lambda^5 \left(e^{\frac{hc}{\lambda \sigma T}} - 1 \right)} \tag{14}$$

where h is Planck's constant, c is the speed of light, and σ is Stefan-Boltzmann constant. Because of the Gaussian heat input and movement of the laser beam, the surface temperature, T, within the pyrometer sampling area is not uniform, and neither is $I(\lambda, T)$. Thus, to carry out the integration of equation (13), approximations are made by dividing the sampling area into n small areas and assuming that T and I are constant within each small area. With these assumptions, equation (13) is reduced to

$$E = \sum_{i=1}^{n} I(\lambda, T_i) \Delta \lambda \Delta A_i \tag{15}$$

where T_i is the surface temperature of the area ΔA_i and n is the number of the small areas within the pyrometer sampling area, A_p. To further simplify the computation, it is assumed that every ΔA_i has the same area, and thus

$$A_p = n \Delta A_i \tag{16}$$

and equation (15) becomes

$$E = \Delta \lambda \Delta A_i \sum_{i=1}^{n} I(\lambda, T_i) \tag{17}$$

To relate the thermal radiation power collected by the pyrometer to the pyrometer temperature reading, an effective temperature, T_{eff}, is introduced as

$$E = \Delta \lambda \Delta A_i \, n \, I(\lambda, T_{eff}) \tag{18}$$

Combining equations (14), (17) and (18), it has

$$T_{eff} = \frac{hc}{\lambda \sigma \ln \left(1 + n \bigg/ \sum_{i=1}^{n} \left(e^{\frac{hc}{\lambda \sigma T_i}} - 1 \right)^{-1} \right)} \tag{19}$$

G. Closed-Loop Temperature Control

T_{eff} in Equation (13) is the effective (nominal) surface temperature of the workpiece as measured by the pyrometer for a given incident laser power. If T_{eff} differs from the desired laser spot temperature, T_p, then the incident laser power is adjusted accordingly to simulate the closed-loop temperature control in the experiment. This is achieved in the simulation by adjusting the laser power from one simulation step to the next using the following equation

$$P_{i+1} = P_i \frac{T_p}{T_{eff}} \qquad\qquad (20)$$

where P_i and P_{i+1} are the incident laser power in the simulation steps i and i+1, respectively. It can be found that this equation allows the surface temperature of the workpiece, T_{eff}, to quickly approach the desired laser spot temperature, reproducing in the simulation the closed-loop temperature control process used in the experiments.

III. Comparison between Simulation and Experimental Results

One of the key criteria for validating the model is to check whether the model can achieve a constant pyrometer temperature (i.e., a constant temperature on the surface of the powder bed) by continuously adjusting the laser input power. Figures 2 and 3 show the comparison between the experimental and simulated pyrometer temperature as a function of the location of the scanning laser beam with a nominal surface temperature of 900 and 1050^{0}C, respectively. It can be seen that the variations in temperature are less than 4% of the desired pyrometer temperatures for all four nominal surface temperatures modeled, which indicates that the closed-loop temperature control in experiments can be simulated with the present model. Furthermore, the pyrometer temperatures achieved by simulations and experiments match quite well.
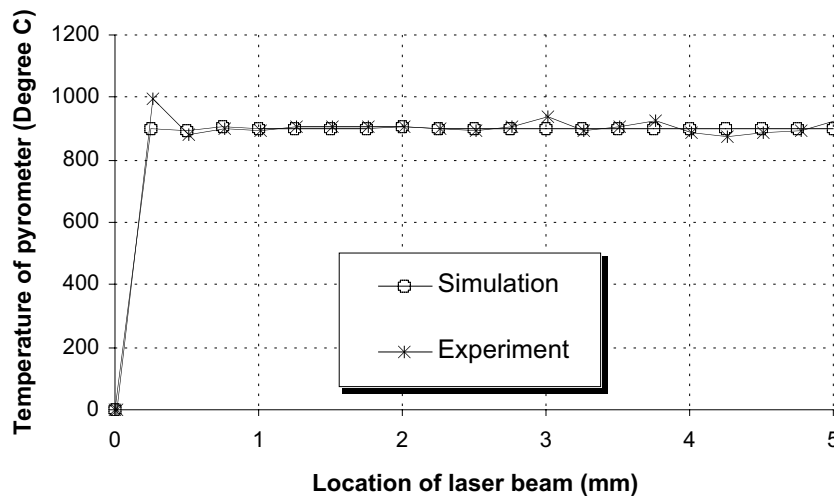

Figure 2. Comparison between the experimental and simulated values of the pyrometer temperature as a function of the location of the scanning laser beam with a nominal surface temperature of 900^{0}C and substrate preheating to 460^{0}C.

The model established is utilized to predict the temperature distribution in the porcelain body during laser densification. Figure 4 show the simulation result with a nominal surface temperature of 1050^{0}C and substrate preheating of 460^{0}C. It is quite clear that the temperature distribution obtained is consistent with the expectation that the highest temperature is located at

the center of the scanning laser beam and the temperature gradually decreases as the location moves away from the center in all directions within the porcelain body. More importantly, when compared with the experimental result (Figure 5), it is found that the predicted temperature distribution pattern matches the measurement quite well. Furthermore, the temperature range predicted also matches the measurement reasonably well. However, a direct comparison of the temperature value between the simulation and experiment is not possible at this stage because of the different laser densification conditions used in Figures 4 and 5. The work on simulations with the identical laser densification condition as the experiment is currently under way and will be published in a forthcoming paper [37].
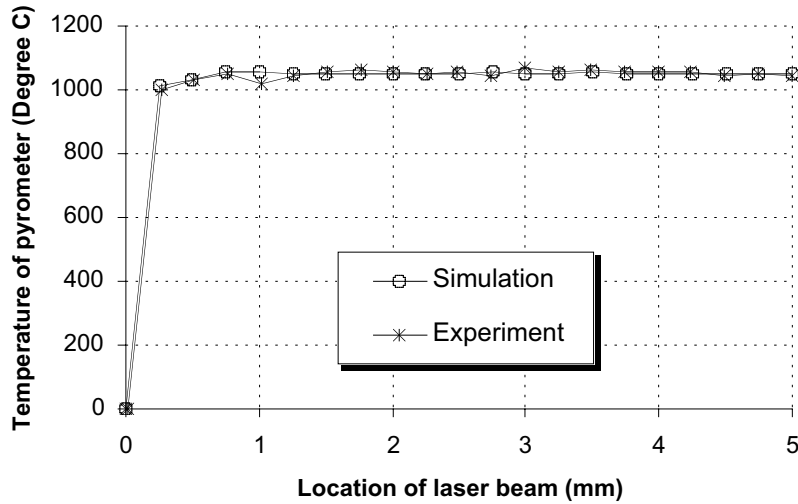

Figure 3. Comparison between the experimental and simulated values of the pyrometer temperature as a function of the location of the scanning laser beam with a nominal surface temperature of 1050^0C and substrate preheating to 460^0C.

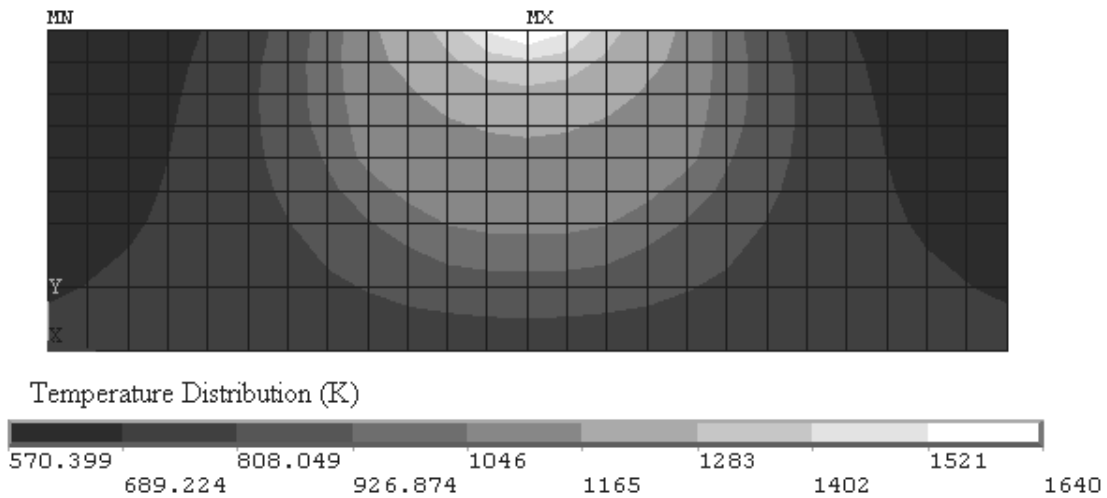

Figure 4. Temperature distribution in the powder bed at the cross section of x = 6.75mm when the laser beam scans to this location with a nominal surface temperature of 1050^0C and substrate preheating to 460^0C.
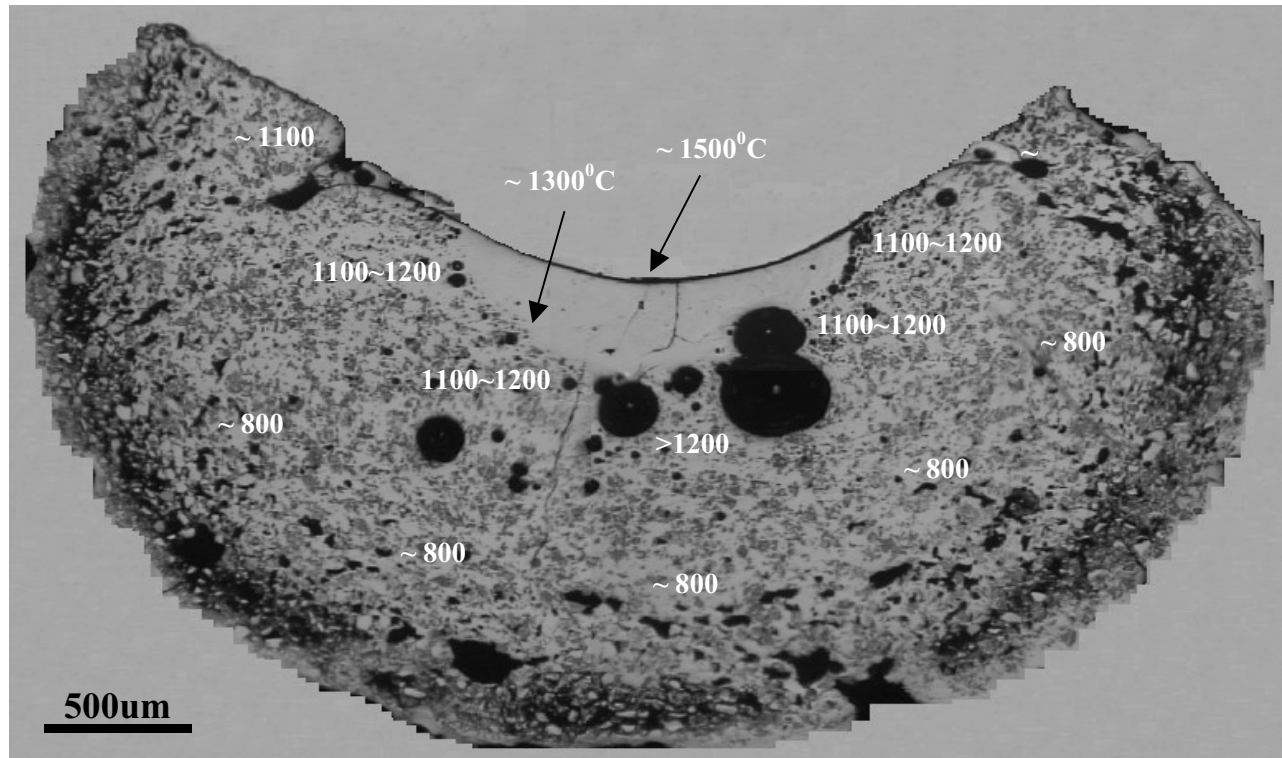
Figure 5. Temperature distribution at the cross section of a porcelain body perpendicular to the laser scan direction during laser densification with a nominal surface temperature of 1100^0C and substrate preheating of 400^0C [37].

IV. Conclusions and Remarks

A 3D finite element model that encompasses the effects of the powder-to-solid transition, laser power density, closed-loop temperature control, temperature- and porosity-dependent thermal conduction and radiation as well as the temperature-dependent natural thermal convection has been developed to carry out the thermal analysis of laser-densified dental porcelain bodies. The temperature distribution in the porcelain body during laser densification has been simulated using this model and is compared with the experiment. The results predicted by the model matches the experiment well, and the model will be used in the future to provide guidance for selecting laser processing conditions to obtain the desired microstructure and geometry of the dense body. This is the first comprehensive model that includes all key parameters in laser densification of powder lines. The model can be extended to simulate many other laser materials processing methods that require consideration of phase transformations, closed loop temperature control, and heat transfer.

242

References

1. Beaman, J.J., Barlow, J.W., Bourell, D.L., Crawford, R.H., Marcus, H.L. and McAlea, K.P., *Solid Freeform Fabrication: A New Direction in Manufacturing*, Kluwer Academic Publishers, MA, 1997.

2. L. Shaw, X.-X. Li, J.-W. Wang, H. L. Marcus, T. B. Cameron, and C. Kennedy, "Dental Restoration through Laser Densification of Dental Porcelain Powder," in *Rapid Prototyping of Materials* (F.D.S. Marquis and D.L. Bourell, Eds.), TMS, Warrendale, PA, 2002, pp. 107-118.

3. J.-W. Wang, X.-X. Li, L. Shaw, H. L. Marcus, T. B. Cameron, and C. Kennedy, "Studies on Slurry Extrusion for Dental Restoration," in the *Proceedings of the 13th Annual SFF Symposium* (D. L. Bourell, J. J. Beaman, R. H. Crawford, H. L. Marcus and J. W. Barlow, Eds.), The University of Texas at Austin, 2002, pp. 83-91.

4. X.X. Li, J.W. Wang, A. Augustine, L.L. Shaw, H. L. Marcus and T. B. Cameron, "Microstructure Evaluation for Multi-Materials Laser Densification of Dental Porcelains", in Proc. of the 12th Annual SFF Symposium, D. L. Bourell, J. J. Beaman, R. H. Crawford, H. L. Marcus and J. W. Barlow, Eds., the University of Texas at Austin, 2001, pp. 195-202.

5. R.K. Chin, J.L. Beuth and C.H. Amon, "Thermomechanical Modeling of Molten Metal Droplet Solidification Applied to Layered Manufacturing", Mech. Mater., 1996, Vol. 24, pp.257-271.

6. C.H. Amon, J.L. Beuth, R. Merz, F.B. Prinz and L.E. Weiss, "Shape Deposition Manufacturing with Microcasting: Processing, Thermal and Mechanical Issues", J. Manufact. Sci. Eng., 1998, 120 [3], pp. 656-665.

7. R.K. Chin, J.L. Beuth and C.H. Amon, "Successive Deposition of Metals in Solid Freeform Fabrication Processes Part 1: Thermomechanical Models of Layers and Droplet Columns", Journal of Manufacturing Science and Engineering, 2001, Vol. 123, No. 4, pp. 623-631.

8. R.K. Chin, J.L. Beuth and C.H. Amon, "Successive Deposition of Metals in Solid Freeform Fabrication Processes Part 2: Thermomechanical Models of Adjacent Droplets", Journal of Manufacturing Science and Engineering, 2001, Vol. 123, No. 4, pp. 632-638.

9. R. Ong, J.L. Beuth and L.E. Weiss, "Residual Stress Control Issues for Thermal Deposition of Polymers in SFF Processes", in Proc. of the 11th Annual SFF Symposium, D. L. Bourell, J. J. Beaman, R. H. Crawford, H. L. Marcus and J. W. Barlow, Eds., The University of Texas at Austin, 2000, pp. 209-218.

10. A. Vasinonta, J.L. Beuth and M.L. Griffith, "A Process Map for Consistent Build Conditions in the Solid Freeform Fabrication of Thin-Walled Structures", Journal of Manufacturing Science and Engineering, 2001, Vol. 123, No. 4, pp. 615-622.

11. A. Vasinonta, J.L. Beuth and R. Ong, "Melt Pool Size Control in Thin-Walled and Bulky Parts via Process Maps", in Proc. of the 12th Annual SFF Symposium, D. L. Bourell, J. J. Beaman, R. H. Crawford, H. L. Marcus and J. W. Barlow, Eds., The University of Texas at Austin, 2001, pp. 432-440.

12. A.H. Nickel, D.M. Barnett, F.B. Prinz, "Thermal Stresses and Deposition Patterns in Layered Manufacturing", Materials Science and Engineering A, 2001, Vol. 317, pp. 59-64.

13. M. Shiomi, M. Matsumoto, K. Osakada, F. Abe, "Two-Dimensional Finite Element Simulation of Laser Rapid Prototyping, Simulation of Materials Processing: Theory, Methods and Applications", in Proc. NUMIFORM 2001 (K. Mori ed.), Toyohashi, Japan, 2001, A.A. Balkema Publishers, pp. 1059-1064.

14. M. Matsumoto, M. Shiomi, K. Osakada and F. Abe, "Finite Element Analysis of Single Layer Forming on Metallic Powder Bed in Rapid Prototyping by Selective Laser Processing", Int. J. Machine Tools & Manufacture, 2002, Vol. 42, pp. 61-67.

15. F. Niebling, A. Otto, "FE-Simulation of the Selective Laser Sintering Process of Metallic Powders", Proceedings of 3rd International Conference on Laser Assisted Net Shaping (LANE2001), Erlangen, Germany, August 2001, pp.371-382.

16. K. Dai and L. Shaw, "Thermal and Stress Modeling of Multi-Material Laser Processing", Acta Mater., 2001, Vol. 49, pp. 4171-4181.

17. K. Dai and L. Shaw, "The Size Effect on Stresses and Distortion of Laser Processed Multi-Material Components", Metall. Mater. Trans. A, Vol. 34A, 2003, pp.1133-1145.

18. K. Dai and L. Shaw, "Distortion Minimization of Laser-Processed Components through Control of Laser Scanning Patterns", Rapid Prototyping Journal, 2002, Vol. 8, No. 5, pp. 270-276.

19. K. Dai and L. Shaw, "Finite Element Modeling for Laser-Assisted Dental Restoration Process," in *Proc. of the 2003 NSF Design*, *Service and Manufacturing Grantees and Research Conference* (R. G. Reddy, Eds.), Birmingham, AL, 2003, pp. 2292-2300.

20. K. Dai, J. Crocker, L. Shaw and H. Marcus, "Modeling of Selective Area Laser Deposition (SALD) and SALD Vapor Infiltration of Silicon Carbide," *Rapid Prototyping Journal*, in press.

21. K. Dai and L. Shaw, "Thermal and Mechanical Finite Element Modeling of Laser Forming from Metal and Ceramic Powders," *Acta Mater*., in press.

22. K. Dai and L. Shaw, "Preheating Effects on Multiple Materials Laser Densification," in the *Proceedings of the 13th Annual SFF Symposium* (D. L. Bourell, J. J. Beaman, R. H. Crawford, H. L. Marcus and J. W. Barlow, Eds.), The University of Texas at Austin, 2002, pp. 392-399.

23. ANSYS Inc., *ANSYS On-Line Reference Manuals: The ANSYS Elements Reference*, Release 6.1, ANSYS Inc., Canonsburg, PA, 2002.

24. Y. S. Touloukian and D.P. DeWitt, *Thermophysical Properties of Matter, Volume 8, THERMAL RADIATIVE PROPERTIES: Nonmetallic Solids*, IFI/Plenum, New York, NY, 1972.

25. Y. S. Touloukian, R.W. Powell, C.Y. Ho, and P.G. Klemens, *Thermophysical Properties of Matter, Volume 2, THERMAL CONDUCTIVITY: Nonmetallic Solids*, IFI/Plenum, New York, NY, 1970.

26. Y.S. Touloukian and E. H. Buyco, *Thermophysical Properties of Matter, Volume 5, SPECIFIC HEAT: Nonmetallic Solids*, IFI/Plenum, New York, NY, 1970.

27. S.J. Schneider, *Engineered Materials Handbook, Volume 4: Ceramics and Glasses*, ASM International, Metals Park, OH, 1991.

28. J. R. Mackert, M. B. Butts, R. Morena and C. W. Fairhurst, "Phase Changes in a Leucite-Containing Dental Porcelain Frit", *J. Am. Ceram. Soc*., 1986, 69[4], C-69 - C-72.

29. S. S. Sih and J. W. Barlow, "The Prediction of the Thermal Conductivity of Powders", in the *Proc. of 1995 Solid Freeform Fabrication Symposium* (H. Marcus, J. Beaman, D. Bourell, J. Barlow, and R. Crawford, eds.), The University of Texas at Austin, 1995, pp. 397-401.

30. S. S. Sih and J. W. Barlow, "Measurement and Prediction of the Thermal Conductivity of Powders at High Temperature", in the *Proc. of 1994 Solid Freeform Fabrication Symposium* (H. Marcus, J. Beaman, J.Barlow, D. Bourell and R. Crawford, eds.), The University of Texas at Austin, 1994, pp. 321-329.

31. S. S. Sih and J. W. Barlow, "Emissivity of Powder Beds", in the *Proc. of 1995 Solid Freeform Fabrication Symposium* (H. Marcus, J. Beaman, D. Bourell, J. Barlow, and R. Crawford, eds.), The University of Texas at Austin, 1995, pp. 402-408.
32. D.R. Poirier and G.H. Geiger, *Transport Phenomena in Materials Processing*, The Minerals, Metals and Materials Society, Warrendale, PA, 1994.
33. E.U. Schlunder (Editor-in-Chief), *Heat Exchanger Design Handbook*, Hemisphere Publishing Corporation, New York, NY, 1983.
34. J. Mazumder and A. Kar, *Theory and Application of Laser Chemical Vapor Deposition*, Plenum Publishing Co., New York, NY, 1995.
35. Y.W. Zhang, *Thermal Modeling of Advanced Manufacturing Technologies: Grinding, Laser Drilling, and Solid Freeform Fabrication*, Ph.D. thesis of the University of Connecticut, 1998.
36. E.U. Schlunder (Editor-in-Chief), *Heat Exchanger Design Handbook*, Hemisphere Publishing Corporation, New York, NY, 1983.
37. X.-X. Li and L. Shaw, "Phase Transformation and Microstructure of Dental Porcelain Powder in Laser-Assisted Rapid Prototyping Processes," to be submitted to Dental Mater.